Growth and electronic structure of some monovalent metals on TiS$_2$(001)

Growth and electronic structure of some monovalent metals on TiS₂(0 0 1)

H H Weitering and T Hibma

Laboratory of Inorganic Chemistry, Materials Science Centre, University of Groningen, Nijenborgh 16, 9747 AG Groningen, The Netherlands

Abstract. The epitaxial growth of Ag on TiS₂(0 0 1) is characterized using reflection high-energy electron diffraction (RHEED), low-energy electron diffraction (LEED) and Auger electron spectroscopy (AES). Ag grows in the (1 1 1) orientation epitaxially on TiS₂(0 0 1) with Ag[1 1̄ 0]‖TiS₂[1 0 0]. The growth mode belongs to the Volmer–Weber type, which means that Ag forms three-dimensional clusters on top of TiS₂(0 0 1). Ag also diffuses slowly into the substrate. The evolution of the electronic structure during this intercalation process is studied in detail with angle-resolved ultraviolet photoelectron spectroscopy (ARUPS) and x-ray photoelectron spectroscopy (XPS). We observed a striking difference between surface Ag and subsurface or intercalated Ag. We conclude that Ag atoms on TiS₂(0 0 1) have little interaction with the substrate, while upon intercalation charge transfer takes place from Ag to TiS₂. For comparison, we also studied Na and K at the TiS₂(0 0 1) surface. At low temperature (−140 °C), Na deposition results in an ordered (√3 × √3)R30° superstructure. Na and K intercalation proceeds very rapidly. The Ti 2p core-level spectra provide additional evidence that charge transfer has taken place after deposition and intercalation of Ag, Na and K.

1. Introduction

Layered transition-metal dichalcogenide (TMDC) compounds exhibit a wealth of interesting physical and chemical properties, which are due to their two-dimensional crystal structures [1]. TMDC compounds are built up of chalogen–metal–chalcogen sheets, which are held together by weak van der Waals forces. Cleavage of single TMDC crystals occurs along the so-called van der Waals gap and yields an almost defect-free, hexagonally close-packed chalcogenide surface without dangling bonds [2]. Particularly, the chemical inertness of TMDC surfaces makes them ideal model systems for studying substrate–adsorbate interactions and epitaxial growth.

The epitaxial growth of metals on TMDC surfaces has been extensively studied by *in situ* electron microscopy for many years [3, 4], but did not attract much attention in modern surface science for a long time. However, nowadays, semiconducting TMDC compounds are considered as ideal substrates for the fabrication of abrupt metal–semiconductor interfaces with a low concentration of defects [5–8]. By investigating such model interfaces with different surface science techniques, attempts were made to clarify the interplay between interface chemistry and Schottky barrier formation.
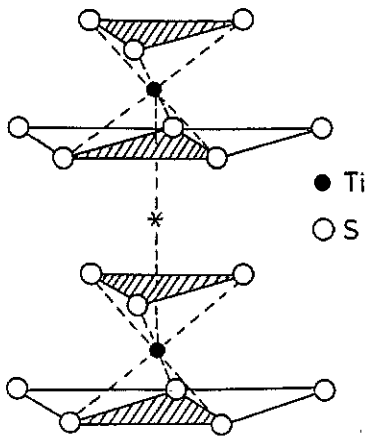
H H Weitering and T Hibma

Figure 1. Simple crystal structure of a layered TMDC compound. The empty space between the sandwiches is the van der Waals gap. The stacking of the sandwiches may be different for various TMDC compounds. If Ag intercalates into TiS_2, it will occupy an octahedral site in the van der Waals gap. This site is marked by an asterisk.

Recently, semiconducting molybdenum and tungsten chalcogenides were used as substrates for the growth of different metallic overlayers [5–11]. Based on photoemission experiments, different authors argued whether chemical reactions at the interface take place or whether abrupt metal–semiconductor interfaces are formed. Core-level photo-emission has been applied to infer the Schottky barrier height at such abrupt metal–semiconductor interfaces, and it has been argued that in these cases the Schottky barrier height approaches the Schottky limit [5–11]. However, photoelectron spectroscopy may not be a suitable technique to study the interface of these systems, because many metals tend to form three-dimensional islands during overlayer growth (Volmer–Weber growth mechanism) [12, 13]. Because photoelectron spectroscopy is a surface-sensitive tech-nique, it probably probes the island surfaces and the bare regions between the islands instead of the interface itself. Therefore, at least a detailed characterization of the surface structures and overlayer growth is required for a definite interpretation of the photoemission results. Unfortunately, the importance of such a characterization has often been underestimated [8, 14].

The growth of metals on layered compounds also has very interesting aspects from a totally different point of view. The deposited metal may diffuse into the van der Waals gap of the substrate (figure 1). This so-called intercalation has important consequences for the electronic structure and physical properties of the TMDC host compound [15, 16]. Intercalation compounds are normally prepared by chemical or electrochemical methods. However, by studying the diffusion of the deposited metal into the host with, for example, photoelectron spectroscopy, one is able to follow the changes in the electronic structure during intercalation [14]. This method may provide more insight into the mechanism and driving force for intercalation. It may also be a test for electronic structure calculations on intercalation compounds.

The electronic structure of the TMDC host compounds is characterized by a broad and fully occupied valence band, which is mainly composed of chalcogen s and p states, and by a rather narrow empty or partially filled conduction band, which is mainly composed of transition-metal d states (see e.g. [17]). Intercalation of TMDC compounds will affect their electronic structure. Band-structure calculations of Dijkstra *et al* on monovalent-metal intercalates of the layered TMDC compound TiS_2 showed that intercalation of TiS_2 with Li, Na and Ag is accompanied by charge transfer from the metal to the conduction band of the host [18]. Also, the Ti 3d/S 3p gap increases for the alkali-metal intercalates

but vanishes for the Ag intercalation compound. The direct interaction between the sulphur atoms of the successive TiS$_2$ sandwiches decreases as a result of the larger *inter*-sandwich distances in the intercalation compound.

The electronic structure of TiS$_2$ was successfully studied by angle-resolved ultraviolet photoelectron spectroscopy (ARUPS) [19, 20]. Generally, for all layered TMDC compounds, the comparison between the experimentally obtained dispersion of the valence electrons parallel to the surface and the calculated band structure is facilitated by their quasi-two-dimensional electronic structure. Most energy bands have only little dispersion perpendicular to the surface. In principle, similar ARUPS studies could be performed on intercalated materials. A comparison with the electronic structure of the host compound should provide information about the changes in electronic structure that accompany intercalation. However, the intercalated crystals usually have very small sizes and the cleavage occurs along cracks, which makes these crystals not very suitable for ARUPS studies [14, 21].

Instead, Starnberg and Hughes [14] used ARUPS to study the evolution of the electronic structure during Ag intercalation into TiS$_2$ after deposition of different amounts of Ag onto TiS$_2$(0 0 1). Their main conclusions were that the silver donates charge to the d band of the host and that the dispersion of the sulphur-derived p states decreases by intercalation. This must be due to the larger *inter*-sandwich distances in the intercalated material. However, their study was not very complete and a detailed surface characterization was lacking.

In this paper we extend the preliminary investigations of Starnberg and Hughes and present a more detailed surface characterization of epitaxial Ag layers on TiS$_2$(0 0 1). For this purpose, we used low-energy electron diffraction (LEED), reflection high-energy electron diffraction (RHEED) and Auger electron spectroscopy (AES). In addition, x-ray photoelectron spectroscopy (XPS) and ARUPS were used to reveal the electronic differences between surface and subsurface (intercalated) Ag. For comparison, we also deposited Na and K onto TiS$_2$(0 0 1). These overlayers were studied by RHEED and XPS.

The remainder of this paper is organized as follows. After a description of the experimental procedures, we will discuss the structure and growth of Ag, Na and K on TiS$_2$(0 0 1). Thereafter, we will present and discuss the ARUPS spectra of the Ag/TiS$_2$(0 0 1) surface. Core-level spectra obtained after deposition of Ag, Na and K will be presented at the end of this paper.

2. Experimental details

TiS$_2$ powder was obtained by mixing nearly stoichiometric amounts of Ti and S in evacuated quartz tubes, followed by heating at 800 °C for one week. In order to obtain nearly stoichiometric TiS$_2$, a small amount of excess sulphur was added to correct for the amount of sulphur present in the gas phase at 800 °C. X-ray powder diffraction (Guinier–Hägg) revealed that the powder was single-phase TiS$_2$ and all reflections could be indexed on the basis of a hexagonal unit cell with the following unit-cell parameters: $a = 3.408$ Å and $c = 5.696$ Å. Single crystals were grown from the powder by iodine vapour transport (900 → 700 °C; 3 mg I$_2$/cm^3). The iodine was removed afterwards by rinsing the crystals with ethanol. The crystals are hexagonal platelets having a gold-coloured metallic lustre. Typical crystal sizes were about $5 \times 5 \times 0.1$ mm^3. According to chemical analysis, the deviation from the stoichiometric ratio was less than 1%.

The crystals were glued onto the sample holder with silver epoxy and dried at about 80 °C for 2 h in order to remove organic residues. An adhesive tape was mounted onto the sample surface and the samples were brought into the preparation chamber of the ultra-high-vacuum (UHV) system. The typical pressure inside the preparation chamber was between 10^{-9} and 10^{-8} mbar. It took about 24 h before the tape was thoroughly outgassed and the pressure was recovered. By tearing off the adhesive tape, the crystal was cleaved and a fresh (0 0 1) surface was obtained.

The characterization of the surfaces and thin films was performed in a molecular-beam epitaxy (MBE) system, equipped with an Ag evaporation source and SAES alkali dispenser sources (Na and K). During the overlayer growth, surface structures were studied with RHEED (15 keV). A reverse-view LEED facility was mounted in a separate chamber attached to the MBE system. Consequently, LEED studies as a function of coverage could only be realized by transporting the sample after each evaporation event. RHEED and LEED patterns could be recorded by means of a CCD camera and were subsequently digitized by use of a personal computer. Coverage-dependent Auger spectra were recorded without transporting the sample. Therefore the coverage-dependent AES and LEED experiments were carried out on different samples. We used a double-pass cylindrical mirror analyser (CMA) with interior electron gun (operated at 3 keV) for analysis and excitation of the Auger electrons, respectively. By modulating the analyser voltage and using phase-sensitive lock-in detection, Auger data were recorded as derivative spectra. Peak intensities were obtained after numerical integration, assuming a linear background. Because the Ag atoms form three-dimensional clusters on the TiS_2(0 0 1) surface, coverage-dependent Auger measurements cannot be used for a straightforward determination of the evaporation rate. However, by applying a simple growth model, the evaporation rate could be obtained as a fitting parameter from the coverage-dependent Auger measurements (see next section). The growth of Ag, Na and K was also studied at low temperature (-140 °C) using RHEED.

ARUPS measurements and angle-resolved XPS measurements were performed in an ADES 400 spectrometer, equipped with an angle-resolving hemispherical energy analyser operated in the retarding mode. We used energy resolutions of about 0.1 eV (He I), 0.25 eV (He II) or 1.1 eV (XPS). The angle resolution is estimated to be ±2°. This system was also equipped with gas-discharge lamp, producing unpolarized He I and He II radiation or Ne I radiation (21.2, 40.8 and 16.8 eV, respectively) and with an x-ray source producing Al Kα and Mg Kα radiation (1486.6 and 1253.6 eV, respectively). A conventional LEED apparatus was used to select a specific azimuthal orientation of the crystal for the ARUPS experiments. The evaporation source was filled with Ag and was mounted in a separate preparation chamber. For each evaporation event, the sample had to be transported from the main chamber to the preparation chamber and vice versa. Therefore, we did not attempt to characterize the overlayer growth in this system very carefully because the transport and realignment of the sample seriously affects the reproduction of the measurements. As will be shown later, the absolute coverage is not a very important parameter for the interpretation of the photoemission results. Therefore we will only specify the overall surface composition as measured with XPS.

XPS measurements with improved resolution were performed in a UHV system equipped with a small-spot monochromatic x-ray source (Al Kα, 1486.6 eV), a hemispherical analyser and a multichannel detector. The best resolution obtainable with this apparatus was about 0.65 eV as determined by measuring the Fermi edge of silver. The spot size of the x-ray beam could be adjusted. The minimum spot size is 150 μm, so that very small crystals can be studied with XPS. Therefore, we were also able to perform high-resolution XPS measurements on a small crystal of $Ag_{0.35}TiS_2$ [22]. The deposition of Ag,
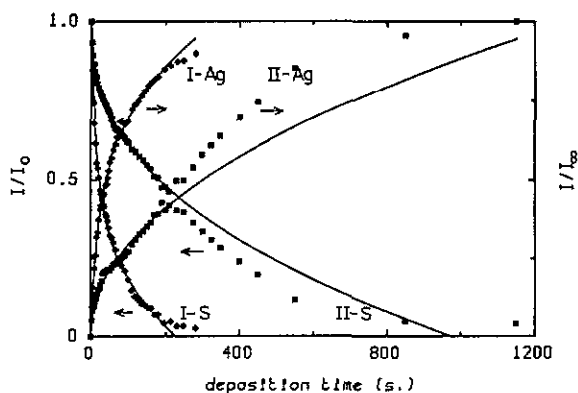
Figure 2. Evolution of the sulphur $L_{23}VV$ and silver $M_{45}VV$ Auger intensities as a function of evaporation time for samples I and II. Even at a deposition time of 1150 s, the Ag Auger signal of sample II did not reach its saturation value. For convenience, the Ag signal at this point is taken as I_x. The left and right scales are identical. Full curves are the result of a non-linear least-squares fitting procedure, using equations (1)–(4). Parameter values are listed in table 1.

Na and K was performed in a separate preparation chamber using similar evaporation sources as mentioned before. Like in the ADES system, the sample had to be transported for each evaporation event. The evaporation rate in this system was approximately equal to that in the ADES 400 system.

3. Epitaxial growth

3.1. Growth mechanism

After cleavage in UHV, the TiS₂(0 0 1) surface was investigated with Auger spectroscopy. The amount of impurities like oxygen and carbon at this surface was below the detection limit of the Auger equipment. The growth mode of Ag on TiS₂(0 0 1) was investigated by measuring the sulphur $L_{23}VV$ and silver $M_{45}VV$ Auger intensity as a function of evaporation time. The results are displayed in figure 2 for two different samples. These two samples exhibit a quite different growth behaviour. We also recorded Auger curves of a third sample. The evolution of the Auger intensity of this sample was again different from those displayed in figure 2. The substrate Auger intensity of sample I almost vanished after about 250 s of deposition time, while for sample II it took more than 800 s. No clear linear segments are observed in this plot, which means that the overlayer growth does not proceed layer by layer. However, the Auger plot of sample II does show a kink in the adsorbate Auger intensity, but this kink cannot be associate with a monolayer break because the adsorbate intensity does not increase linearly below the kink. If we calculate the escape depth λ of the Ag Auger electrons from the intensity ratio I^{Ag}/I_x at the kink, we obtain a value for λ of about 11 Å, which is also quite large. A more reasonable value for λ would be 8 Å [23]. In addition, we do not observe a similar kink in the substrate Auger intensity. We therefore conclude that Ag probably grows according to the Volmer–Weber mechanism, i.e. the Ag atoms form three-dimensional islands on top of the substrate surface. LEED observations also point towards a Volmer–

Table 1. Listing of fitting parameters for the Auger data in figure 2. The escape depth λ of the Auger electrons is estimated from the universal curve of λ versus kinetic energy [23]. For the fitting procedure, we used values of 6 Å for the S L_{23}VV Auger electrons and 8 Å for the Ag M_{45}VV Auger electrons. The deviations are rough estimates. ML = monolayer.

Sample	Auger line	Deposition rate (ML s^{-1})	a	p
I	S L_{23}VV	0.09 ± 0.02	0.38 ± 0.05	0.24 ± 0.05
	Ag M_{45}VV	0.09 ± 0.02	0.31 ± 0.05	0.29 ± 0.05
II	S L_{23}VV	0.11 ± 0.02	0.10 ± 0.02	0.41 ± 0.07
	Ag M_{45}VV	0.10 ± 0.02	0.06 ± 0.02	0.47 ± 0.07

Weber growth mechanism, as will be discussed later. The difference between the Auger curves for the two samples indicates that the morphology of the metallic overlayer differs from sample to sample. This must be due to differences in surface quality, which is of course quite conceivable because the density of nuclei will be strongly dependent on the density of defects or steps at the surface.

Because the overlayer growth does not proceed in a layer-by-layer fashion, it is not possible to infer a coverage in monolayers directly from these Auger measurements. However, the Auger intensity can be fitted by applying a simple growth model using the evaporation rate as an adjustable parameter. From the theoretical fit, the absolute evaporation rate can be deduced. We will explore this in more detail below.

According to Zhu *et al* [24], the relation between the mean height of the islands and the total amount of deposited adsorbate atoms can be described by a power law, provided that nucleation only takes place within a very short time at the beginning of epitaxial growth:

$$x = a(t_0\Theta)^p \tag{1}$$

$$h = (1/a)(t_0\Theta)^{1-p} \tag{2}$$

where a and p are free parameters. The fraction of the surface covered by islands is x. The thickness of one atomic layer of Ag (2.36 Å) is t_0 and the total number of full monolayers of Ag is Θ. Note that the nominal layer thickness $hx = t_0\Theta$, as it should be. For a quasi-isotropic growth mode, $h/\sqrt{x}$ will remain constant, and it is easy to show that in this case the power p equals 2/3. The physical significance of the parameter a has been discussed by Zhu *et al* [24]. With the aid of equations (1) and (2) we will fit the Ag and S Auger intensity using the following equations:

$$I^S/I_0 = (1 - x) + x\exp(-h/\lambda) \tag{3}$$

$$I^{Ag}/I_x = x[1 - \exp(-h/\lambda)] \tag{4}$$

where I_0 and I_x denote the initial S intensity and Ag saturation intensity, respectively. The escape depth λ includes a factor 0.74, which accounts for the acceptance angle of the cylindrical mirror analyser and is different for the Ag and S Auger electrons. The full curves in figure 2 are fits, using equations (1)–(4). The fitting parameters are displayed in table 1. The best fits are obtained using data in the interval between 0 and 200 s. Above 200 s, the fit clearly deviates from the experimental data. For sample I this deviation is probably due to coalescence of the islands, which means that the lateral

growth of the islands ceases. For sample II, this simple explanation cannot hold because the Ag intensity increases faster above 200 s than predicted by the model. Therefore, it must be concluded that in this region the overlayer growth proceeds in a more complex way than the model suggests.

At 200 s of deposition time, the mean height of the Ag islands is about 25 and 60 Å for samples I and II, respectively, and the fraction of the covered surface is about 80% and 50%, respectively. Below 200 s, the thin-film growth can be satisfactorily described by this simple model although the presence of the kink remains a puzzle. From table 1 it can be seen that the power p severely deviates from 2/3, which means that the islands do not adopt a quasi-equilibrium shape during their growth. The evaporation rate, which can be obtained from the fits, is about 0.1 ML s^{-1}. Here, one monolayer (ML) is defined as a hexagonally close-packed (1 1 1) layer. This evaporation rate was also used for the RHEED and LEED experiments (next section).

3.2. Surface structures

3.2.1. Ag deposition at room temperature. The RHEED and LEED patterns of a freshly cleaved TiS$_2$ sample (sample III) were very bright and sharp. As expected, the LEED pattern clearly revealed the threefold symmetry with respect to the c axis of the crystal.

Immediately after starting the Ag deposition, new streaks appeared in the RHEED pattern (figure 3). These streaks fall outside the substrate streaks. These new streaks originate from diffraction by an epitaxial Ag film. The lattice constant of this epitaxial layer is 2.88 Å, which is very close to the interatomic distances in the (1 1 1) plane of bulk Ag. From our RHEED patterns, we conclude that Ag grows epitaxially in the (1 1 1) orientation on TiS$_2$(0 0 1) with Ag[1 $\bar{1}$ 0]‖TiS$_2$[1 0 0].

Sometimes, broad but distinct intensity maxima were observed along the diffraction streaks normal to the shadow edge. These diffuse maxima correspond to bulk-like Bragg reflections of the RHEED beam penetrating small three-dimensional crystallites that are present at the surface. The separation between these maxima along the streak directly yields information about the periodicity normal to the crystal surface. From these transmission patterns, we deduce that the stacking of the epitaxial Ag(1 1 1) layers is ABC, i.e. cubic close-packed. The intensity of these transmission spots depends on the surface roughness, which may differ from sample to sample.

After 20 s of deposition time, all RHEED spots of the substrate had disappeared. The Auger data of samples I and II suggest that at about 20 s only a minor part of the surface will be covered with islands (45% and 14% for samples I and II, respectively). LEED experiments, which are described below, indicate that this is also the case for sample III. The total disappearance of the substrate reflections in the RHEED pattern at about 20 s is probably due to the grazing-incidence geometry (figure 4). From this figure it is seen that the substrate will be shadowed by the three-dimensional clusters. Therefore the substrate reflections in RHEED will fade out very rapidly as the coverage increases. Although in figure 4 the surface is depicted in one dimension, the same argument also applies in two dimensions because the electron beam impinges upon the surface from a fixed direction. For a more quantitative discussion of this subject we refer to Rao *et al* [25].

Our LEED observations on sample III are quite different from the RHEED observations. Up to 20 s deposition time, no Ag spots could be observed in the LEED patterns. Instead, the substrate spots remained visible but became very broad and the background intensity was strongly enhanced. After about 60 s weak but very sharp silver spots were
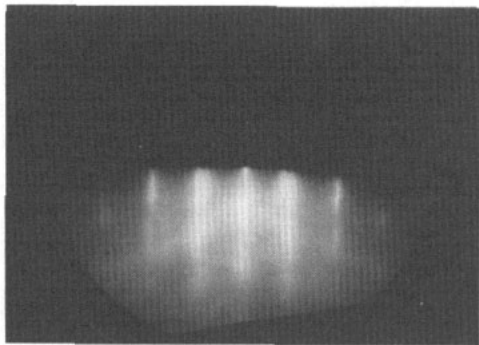
Figure 3. RHEED pattern (15 keV) of TiS$_2$(001) with a small amount of epitaxial Ag(1 1 1). The incident beam is along the [1 0 0] azimuth. The outer streaks are due to diffraction by small Ag(1 1 1) crystallites.
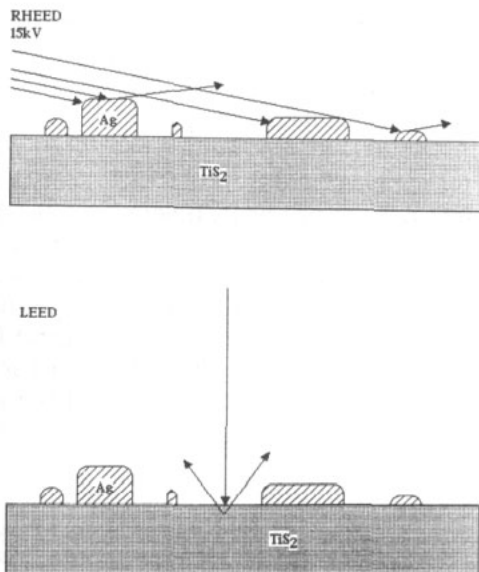

Figure 4. Different diffraction geometries for LEED and RHEED. At grazing incidence (RHEED), the substrate will be shadowed by the adsorbate islands and the substrate spots will fade out very rapidly. At normal incidence (LEED), substrate spots remain visible longer. Note that this drawing is a one-dimensional representation.

observed while the TiS$_2$ spots remained broad (figure 5). At about 200 s the substrate spots were still clearly visible. This observation supports our conclusions from the Auger measurements, namely that the thin-film growth proceeds in islands.

The substrate spots retained their trigonal symmetry but the silver showed hexagonal symmetry. Because the RHEED transmission spots show that the islands are cubic close-packed, the hexagonal symmetry of the diffraction spots indicates that ABC and ACB type domains are present in roughly equal amounts.

In summary, epitaxial FCC Ag islands are formed immediately after starting the deposition of Ag. These islands give rise to sharp diffraction streaks in RHEED but cannot be seen in LEED. The substrate spots in LEED become very broad, whereas weak but sharp diffraction spots of the Ag islands were observed only after prolonged deposition.

The evolution of the width of the diffraction spots is in contrast to what we expect because the width of the diffraction spots is inversely proportional to the size of the scattering area. Therefore, at low coverages, small island sizes should give rise to broad adsorbate spots and sharp substrate spots. However, immediately after the beginning of epitaxial growth, the RHEED streaks belonging to the adsorbate do not show significant broadening. This means that the island size must be at least of the order of the coherence width of the RHEED experiment, which is typically 100–500 Å [26]. Such large domains should also give rise to sharp diffraction spots in the LEED pattern (the coherence width of the LEED experiment is typically 100 Å [26]). Because the adsorbate spots cannot be initially observed with LEED, there must be a difference in detection limit for the islands in the RHEED and LEED experiments. This is probably due to the differences in diffraction
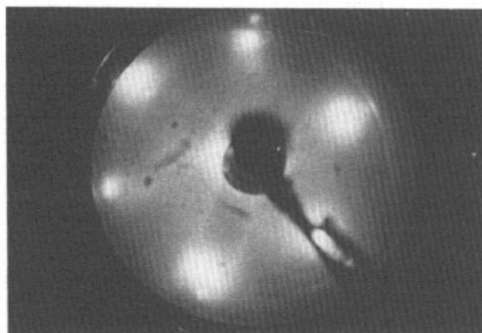
Figure 5. LEED pattern of the Ag(1 1 1)/TiS₂(0 0 1) surface, showing broad substrate spots and sharp adsorbate spots. The intensity of the substrate spots exhibits threefold symmetry, while the intensity of the adsorbate spots exhibits hexagonal symmetry.
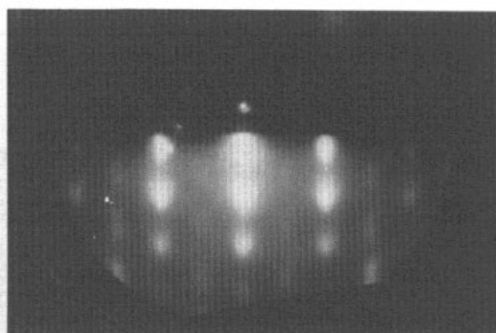
Figure 6. RHEED transmission pattern of epitaxial Ag(1 1 1) crystallites after deposition at $-140\,°C$. The incident beam is along the $[1\,\bar{1}\,0]$ azimuth of the substrate. The vertical distances between the Bragg spots is equal to $3c^*$, where c^* is the reciprocal c axis for an ABC stacked close-packed structure in hexagonal setting.

geometry (figure 4). Therefore, as soon as the islands are detected with LEED, the Ag diffraction spots will always be sharp.

No simple explanation can be given for the broadening of the substrate spots. In general terms, the broadening must be due to some effect that causes a fragmention of the surface into regions that are small with respect to the coherence length of LEED. This might be due to surface roughness, caused by adsorption of Ag atoms or by intercalation. Another possibility is that some distribution of Ag islands might exist, which divide the substrate surface into very small regions.

It is obvious that, in order to make a definite interpretation of these diffraction experiments, one must make a quantitative comparison between the LEED, RHEED and Auger measurements. For this purpose, all these experiments should be performed on the same sample at a fixed position. For a more quantitative and detailed discussion about this matter, we refer to Rao *et al* [25].

Finally we want to quote some previous experiments on metals on layered compounds. Starnberg and Hughes [14] also investigated epitaxial Ag layers on TiS₂(0 0 1). Because they did not observe adsorbate reflections in the LEED pattern, they concluded that the Ag grows in registry with the substrate, despite the 15% lattice mismatch. Our RHEED experiments refute their conclusion. It is clear that it is necessary to use both RHEED and LEED for studying overlayer structures. Recently Jaegermann *et al* [8] concluded on the basis of their LEED observations that Ag grows epitaxially in the (1 1 1) orientation in registry with the WSe₂(0 0 1) substrate, despite a large mismatch. We suggest that, also in this case, RHEED may provide additional evidence of whether or not this is true.

3.2.2. Ag, Na and K deposition at low temperature. X-ray diffraction experiments on a silver intercalated bulk crystal $Ag_{0.35}TiS_2$ revealed that, below 300 K, silver atoms form an ordered arrangement by occupying one-third of the available octahedral sites in the van der Waals gap [22]. The ordering of the silver atoms gives rise to a $\sqrt{3} \times \sqrt{3}$ superstructure. Superstructures are also observed in Na and K intercalates of TiS₂ [15].
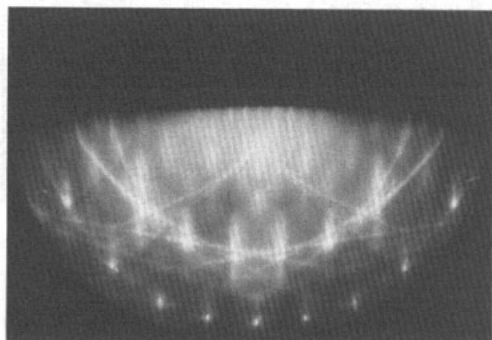
Figure 7. RHEED pattern of Na on $TiS_2(001)$ at $-140\,°C$. Thin streaks evolve between the substrate streaks and are due to the formation of an $a\sqrt{3} \times a\sqrt{3}$ superstructure. These streaks disappeared during irradiation with the RHEED beam. The incident beam is along the $[1\bar{1}0]$ azimuth of the substrate.
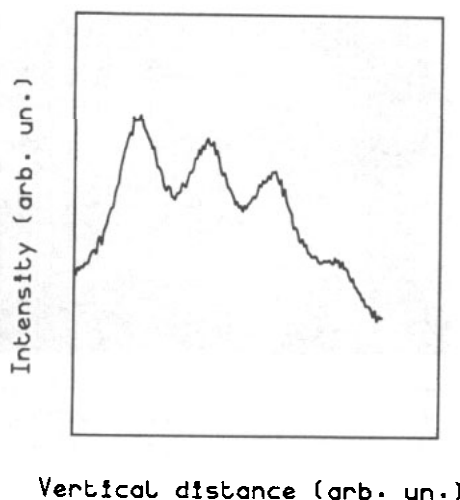

Figure 8. Vertical scan along the $(1, 1)$ diffraction streak after deposition of Na. Distinct maxima are easily recognized and are due to three-dimensional diffraction of the RHEED beam at a rough surface. The instances between these Bragg spots is equal to c^*, where c^* is the reciprocal c axis of TiS_2. The c axis becomes elongated as foreign atoms are intercalated.

In these compounds the stacking of the sandwiches is changed [27, 28]. The ordering of the metal atoms can be explained with simple electrostatic arguments. Intercalation is accompanied by partial or complete charge transfer of the outer valence electron of the metal to the host. Coulomb interactions between the intercalated metal ions may result in the formation of ordered superstructures [15].

We investigated whether such superstructures are also formed at the surface of $TiS_2(001)$. As discussed previously, room-temperature deposition of Ag always yielded epitaxial (111) bulk type layers and superstructures were not observed. Apparently, at the surface charge transfer does not occur. Even if the much more electropositive elements Na and K are deposited at room temperature, no superstructure reflections are observed. Instead, the diffuse background intensity became very strong, which indicates that the surface became very rough or disordered.

Low-temperature deposition $(-140\,°C)$ yielded quite different results. Ag deposition resulted in a transmission type RHEED pattern (figure 6), which indicates that island growth at low temperature causes much more surface roughness than room-temperature deposition. Again, the Ag grows in the (111) orientation with an ABC type stacking of the (111) planes. Further deposition resulted in diffraction rings, which shows that polycrystalline Ag is formed. Deposition of Na resulted in a $(\sqrt{3} \times \sqrt{3})R30°$ superstructure (figure 7). However, this structure was unstable during irradiation with the RHEED beam, and an absolute determination of the coverage was impossible. It is likely that the Na intercalates very fast because of local heating by the electron beam. Indeed, on several occasions, transmission maxima along the substrate streaks were visible (figure 8). The transmission maxima again indicate that the surface became rough. From the horizontal separation between the transmission spots, the lattice
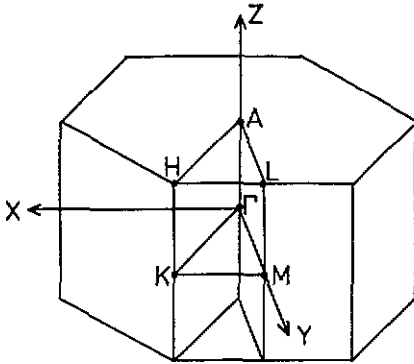
Figure 9. Brillouin zone of TiS$_2$.

parameters can be deduced. From the vertical separations between the diffraction spots, we determined the period perpendicular to the surface to be 6.4 ± 0.1 Å. This value was quite reproducible for other Na/TiS$_2$ samples. It is much larger than the c axis of the host (5.696 Å) and is close to the c axis of Na$_{0.33}$TiS$_2$ [27, 28]. Possibly, the stacking of the sandwiches near the surface is changed because Na normally occupies trigonal prismatic sites in Na$_x$TiS$_2$. In that case, the surface layers would probably break up. The resulting roughening or destruction of the surface would account for the high diffuse background and the presence of pronounced transmission spots in the RHEED pattern. Similar transmission spots were also observed after deposition of K, yielding a period of about 7 Å normal to the surface. This very close to the c axis of K$_{0.15}$TiS$_2$ [28]. However, for this system we also obtained values of 7.4 and 7.6 ± 0.1 Å, which are close to the values of KTiS$_2$ (7.61 Å) [28].

4. Angle-resolved ultraviolet photoelectron spectra

Using He I radiation ($\hbar\omega = 21.2$ eV), we recorded spectra along the ΓMLA and ΓKHA planes of the Brillouin zone (figure 9). The initial energies E_i and parallel wavevectors $k_\parallel$ are determined using the following relations [29]:

$$E_{\text{kin}} = \hbar\omega - E_i - \Phi_s \tag{5}$$

$$\hbar|k_\parallel| = \sin\theta \, (2mE_{\text{kin}})^{1/2}. \tag{6}$$

E_i is referred to the Fermi level. E_{kin} is the kinetic energy of the photoelectrons (mass m) and θ is the detector angle with respect to the surface normal. The sample work-function Φ_s is determined by measuring the secondary cut-off in photoelectron spectrum at different sample bias, and varied between 4.5 and 5.5 eV for different TiS$_2$ samples.

4.1. The substrate

The ARUPS spectra of clean TiS$_2$(0 0 1) are displayed in figure 10. The parallel-wavevector dependence of the initial state energies of cleaved TiS$_2$(0 0 1) are shown in figure 11. The dispersion should be compared with band-structure calculations. However, complications may arise because the wavevector perpendicular to the surface k_z is not conserved. If one assumes that the perpendicular wavevector is conserved during the
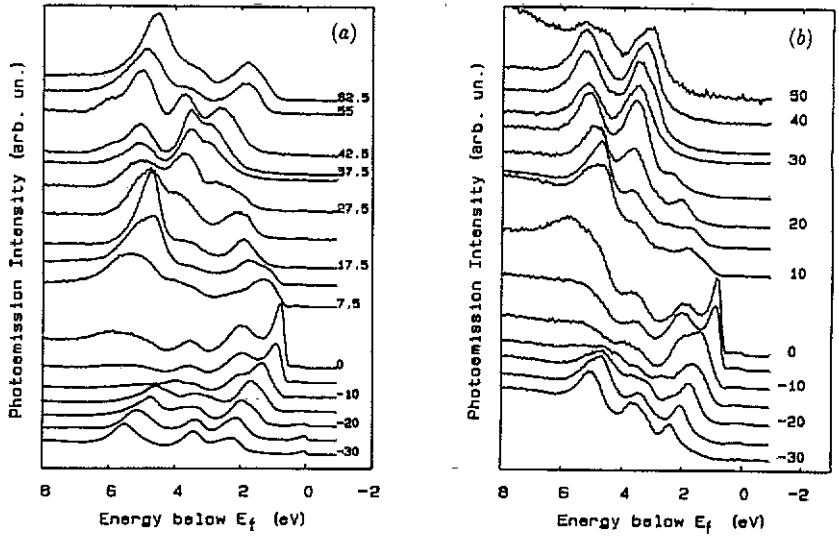
Figure 10. Angle-resolved UPS spectra of cleaved $TiS_2(001)$ along the ΓMLA (*a*) and ΓKHA (*b*) planes of the Brillouin zone. We used unpolarized He I radiation (21.2 eV). The angle of light incidence is $45°$ with respect to the surface normal. Emission angles are given in degrees.
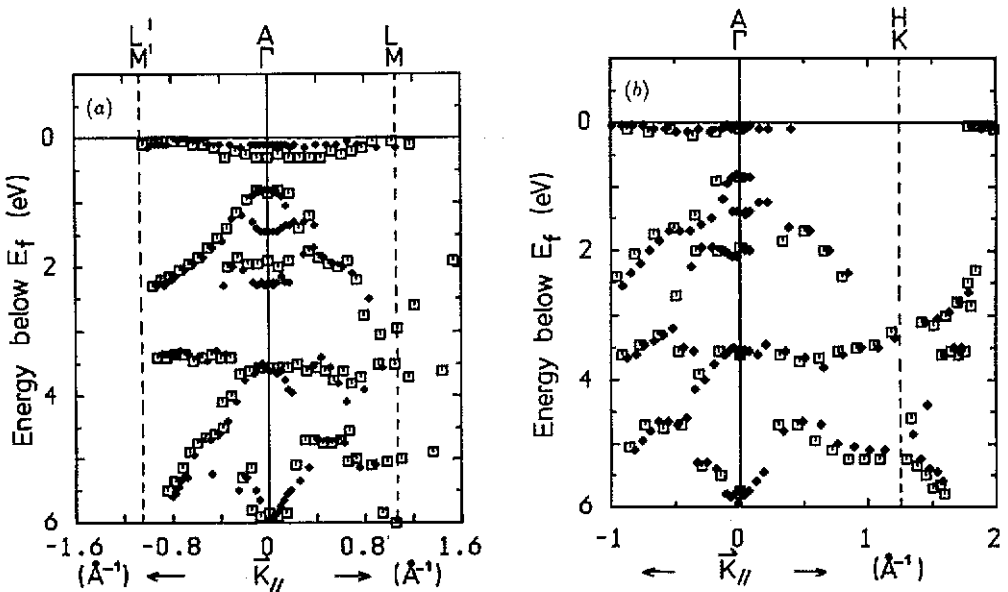
Figure 11. Parallel dispersion of the valence states of clean TiS_2 (□) and Ag/TiS_2 (♦) along ΓMLA (*a*) and ΓKHA (*b*). Data points are calculated by means of equations (5) and (6) using the spectra of figures 10 and 15. An average value of 5 eV was taken for the sample workfunction Φ_s.

photoemission process, k_z can be obtained if the dispersion of the final state is known (direct transitions) [29]. If k_z is completely undetermined, the peaks in the photoelectron spectrum coincide with the maxima in the one-dimensiional density of states along a particular line in the k_z direction (indirect transitions) [30]. Irrespective of the type of photoemission process (direct or indirect transitions), the experimental peak positions should fall within the two-dimensional projected band structure onto the (0 0 1) plane [31]. This procedure has been used by Coehoorn for the related compound TiSe₂. He showed that the experimental dispersions are in fairly good agreement with band-structure calculations [31]. Chen *et al* also measured the experimental dispersion for TiSe₂ and TiS₂ [19], while Barry *et al* investigated stoichiometry effects on the experimental band structure of Ti₁₋ₓS₂ [20]. All these investigations yield a consistent view of the electronic structure of TiS₂ and showed that TiS₂ is a semiconductor with a small indirect band gap of about 0.2 eV. Therefore, our photoemission data do not contribute new aspects to the present understanding. However, we would like to point out that our data are more detailed in the sense that we used smaller angular intervals than others. In addition, we measured the dispersion along the ΓKHA plane. for the sake of comparison with the Ag/TiS₂(0 0 1) system, which will be treated in the next section, a few important aspects of the experimental and theoretical band structure of TiS₂ will be discussed in more detail below.

4.1.1. The dispersionless state at E_F. According to the electronic structure calculations [18, 32], the Ti-derived 3d(t₂g) band reaches its minimum at L, just below E_F, whereas the S-derived 3p states at this point in the Brillouin zone are situated far below E_F. The valence band maximum is found in Γ and is situated slightly *above* E_F. These valence band states are mainly composed of S 3p states. Thus according to the band-structure calculations, TiS₂ is a semi-metal with a very small energy overlap between the S-derived 3p states in Γ and the Ti-derived 3d states at L.

However, our angle-resolved photoemission data show that the valence states at Γ(A) are situated well below E_F and that the Fermi level is pinned by a dispersionless state. The maximum photoemission intensity from the dispersionless state is at E_F observed near the M(L) point. According to the band-structure calculations, the only states that cross the Fermi level near M(L) are the Ti 3d states. Therefore, it is believed that the photoemission intensity at the Fermi level near M(L) arises from partially occupied Ti 3d states [19, 20]. Because all the sulphur-derived valence band states are well below E_F, this probably means that the crystals are *not* stoichiometric. A small amount of excess Ti in the van der Waals gap may be responsible for the partial filling of the Ti 3d states. If these states near M(L) correspond to the conduction band minimum, it can be concluded that stoichiometric TiS₂ is probably a semiconductor with a small energy gap between the filled valence states at Γ(A) and the empty conduction band states near M(L). However, it is questionable whether the states at E_F are true conduction band states, because the lack of dispersion is in severe conflict with the band-structure calculations.

These states persist throughout the whole Brillouin zone, and even at the zone centre some emission is left. A similar dispersionless state has also been observed in a large number of other layered compounds, like MoSe₂ [33], TaS₂, TaSe₂ [34], TiTe₂ [35], TiSe₂ [19, 36] and TiS₂ [19, 20], and has been ascribed to many different phenomena, like radiation satellites [19], an impurity band [37] or many-body effects [35, 36]. Very recently, this dispersionless peak was also observed in the ARUPS spectra of the misfit layer compound (SnS)₁.₂₀TiS₂ [38]. The photoemission intensity from this dispersionless

state in TiS_2 strongly increases when He II radiation is used [37], which supports the view that this state is mainly composed of Ti 3d orbitals throughout the whole Brillouin zone, and excludes the possibility that this emission is due to excitation by a radiation satellite of the He lamp (23.1 eV).

This dispersionless state may represent an impurity state or defect state, possibly related to deviations from stoichiometry, i.e. excess Ti in the van der Waals gap. Recently, real-space images of the $TiS_2(0\,0\,1)$ surface were obtained by use of a scanning tunnelling microscope (STM) [39]. Three types of defects were observed, which could be assigned to Ti interstitials in tetrahedral sites and to octahedral Ti vacancies. Because these images were obtained with a sample bias of 25 mV with respect to the tip, the defect levels must be situated close to the Fermi level and may give rise to a dispersionless feature in the UPS spectrum. On the other hand, Pehlke and Schattke argued that Frenkel type defects in the related compound $TiSe_2$ may be responsible for the occurrence of a localized electronic state at 1.5 eV *below* the Fermi level [40].

An alternative explanation for the appearance of the dispersionless state at the Fermi level was given by De Boer *et al*, who pointed out that this state is observed in many highly polarizable TMDC compounds with d electrons [35]. They argued that a localized quasi-particle may be formed by mixing of one-electron d states with different wave-vectors along ΓM. Electronic polarization and correlation might be responsible for the breakdown of the single-particle picture for the d electrons of many transition-metal dichalcogenides. We will show later that Ag deposition on TiS_2 affects the photoemission from this dispersionless state.

4.1.2. The nature of the valence bands in Γ. Because silver deposition mostly affects the valence bands near the zone centre, we will briefly discuss the normal emission spectra of clean $TiS_2(0\,0\,1)$. Figure 12 shows the normal emission spectra ($|k_\parallel| = 0$) at various excitation conditions. By variation of the angle of light incidence, we obtain information about the symmetry of the initial state wavefunction. From figure 12, we conclude that the states at about 0.8 and 3.5 eV below E_F are excited by the in-plane components of the radiation field and must therefore have p_x, p_y symmetry. The state at approximately 2 eV below E_F is excited by the z component of the radiation field and has p_z symmetry. Also the state at about 6 eV below E_F seems to have p_z symmetry although the inelastic background contributes significantly to the intensity of this peak.

A more precise assignment of the photoemission peaks can be made by a comparison with band-structure calculations. Because the perpendicular wavevector is not conserved during the photoemission process, we have to compare the experimental peak positions at normal emission ($|k_\parallel| = 0$) with the theoretical band structure along ΓA. For this purpose, we will use the band-structure calculations of Dijkstra *et al* [18] (figure 13). From these calculations, the contribution of each basis function to the wavefunctions at Γ can be inferred (table 2) [41]. The Γ_3^+ bands have little dispersion and must be composed of in-plane atomic orbitals. The $\Gamma_3^- - A_3^-$ band is mainly composed of sulphur $3p_x$ and $3p_y$ orbitals, while the $\Gamma_3^+ - A_3^+$ band is mainly composed of sulphur $3p_x$ and $3p_y$ orbitals hybridized with Ti $3d_{xy}$, $3d_{x^2-y^2}$ orbitals. The large dispersion of the $\Gamma_2^- - A_2^-$ and $\Gamma_1^+ - A_1^+$ bands is characteristic for the interaction between successive sandwiches. The $\Gamma_1^+ - A_1^+$ band is composed of sulphur $3p_z$ orbitals with a small admixture of Ti $3d_{3z^2-r^2}$ orbitals, while the $\Gamma_2^- - A_2^-$ band is almost solely composed of sulphur $3p_z$ orbitals. The Γ_1^+ state is composed of S $3p_z$ orbitals, which form bonding combinations between the successive sandwiches. Likewise, the Γ_2^- state is mainly composed of S $3p_z$ orbitals making antibonding combinations between the successive TiS_2 sandwiches [42].
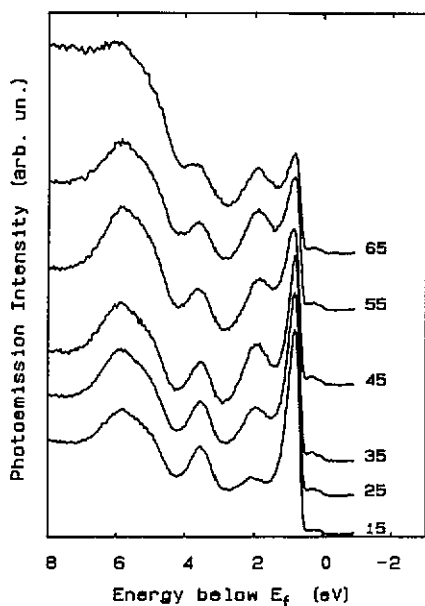
Figure 12. Normal He I emission spectra of cleaved TiS$_2$(0 0 1) at various angles of light incidence α.
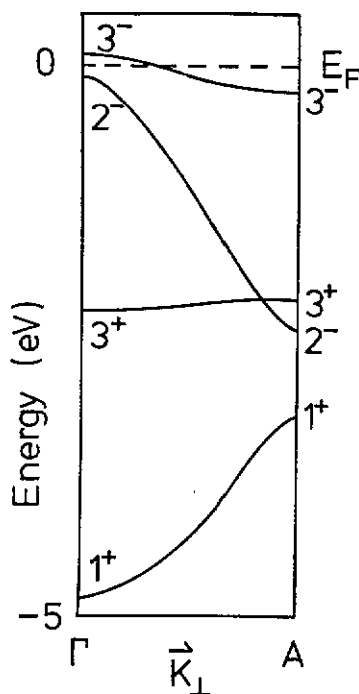
Figure 13. Calculated dispersion along ΓA [18].

Table 2. Population analysis of the wavefunctions in Γ as calculated by Dijkstra *et al* for TiS$_2$ [18, 41]. Only the major contributions are tabulated. The Γ^- states do not mix with the Ti 3d states.

Energy (eV)	Symmetry	Basis functions
−4.83	Γ_1^+	16% 3d$_{z^2}$ + 68% 3p$_z$
−2.20	Γ_3^+	16% 3d$_{xz}$ + 39% 3d$_{x^2-y^2}$ + 44% 3p$_x$
−2.20	Γ_3^+	16% 3d$_{yz}$ + 39% 3d$_{xy}$ + 44% 3p$_y$
−0.07	Γ_2^-	94% 3p$_z$
+0.07	Γ_3^-	94% 3p$_y$
+0.07	Γ_3^-	94% 3p$_x$

Based on the above analysis, we are able to identify the peaks in the photoelectron spectrum at normal emission. The peak at about 6 eV below E_F corresponds to the Γ_1^+–A$_1^+$ band. However, according to the calculations, the bottom of this band is situated at 4.8 eV below the Fermi level. Consequently, the calculated valence bands have to be shifted 1.2 eV downwards with respect to the transition-metal d band in order to obtain reasonable agreement with experiment. The uppermost valence band in the photoemission spectrum has p$_x$, p$_y$ symmetry and must therefore correspond to the Γ_3^-–A$_3^-$ band. Then the emission at 2 eV below E_F, which has p$_z$ character, must correspond to
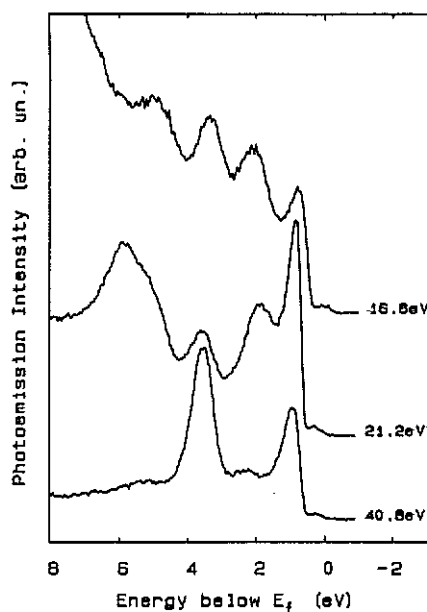
Figure 14. Photoelectron spectra of clean $TiS_2(001)$ at normal emission (ΓA) using different photon energies: Ne I (16.8 eV), He I (21.2 eV) and He II (40.8 eV). The angle of light incidence is 45° in all cases.

Table 3. Coverages of Ag on TiS_2 belonging to the spectra in figures 15–18.

Deposition time (min)	Coverage (ML)	LEED spots	UPS
1	4 ± 2	TiS_2	S 3p
2	8 ± 4	TiS_2	S 3p + Ag 4d
30	>100	TiS_2 + Ag	S 3p + Ag 4d
60	>200	Ag	Ag 4d

the $\Gamma_2^- - A_2^-$ band. Finally, the state at about 3.5 eV below E_F corresponds to the $\Gamma_3^+ - A_3^+$ band.

The Ti 3d orbitals do not contribute significantly to the interlayer bonding. However, substantial Ti 3d character is present in the $\Gamma_3^+ - A_3^+$ band. This is nicely illustrated by our He II spectra (figure 14). Using He II radiation, the ratio of the atomic Ti 3d and S 3p photoionization cross sections is about 6.7, while for He I radiation it is about 1.2 [43]. Therefore, the He II spectrum in Γ mainly reflects the contribution from the Ti 3d states to the valence band region. As expected, the photoemission intensity from the $\Gamma_3^+ - A_3^+$ band dominates the He II spectrum. However, also the emission from the uppermost valence band has substantial intensity, while this state is only composed of S 3p orbitals. To explain this behaviour, a more detailed analysis should be performed including calculations of transition matrix elements.

4.2. Ag on $TiS_2(001)$

Spectra were recorded after deposition sequences of 1, 2, 30 and 60 min. Approximate surface compositions are listed in table 3. Up to 5 min of deposition time, the LEED

pattern only showed a broadening of the substrate spots together with an enhancement of the diffuse background. After 5 min, sharp Ag spots became visible. At 30 min, diffraction spots of the substrate and adsorbate were present with approximately equal intensity. After 60 min, the substrate spots were no longer visible. It will be shown that the absolute coverage is not a critical parameter as far as the peak positions in the UPS spectrum are concerned.

Figures 15–18 show the ARUPS spectra along ΓMLA at different coverages. After a deposition time of 1 min, we also recorded spectra along ΓKHA. At higher coverages, dramatic changes appear in the region 4–6 eV below E_F, which is due to emission from the Ag 4d states (figure 16–18). After 60 min, substrate peaks have disappeared from the UPS spectra (figure 18), and a comparison with literature shows that our spectra are similar to those of the Ag(1 1 1) surface [44]. This confirms our previous conclusions that Ag is present in three-dimensional (1 1 1) oriented islands. At 60 s of deposition time, the Ag 4d emission is still hidden under the substrate photoemission peaks.

The experimental dispersion of the valence states at the Ag/TiS₂(0 0 1) surface is plotted in figure 11. Apart from the changes near the zone centre and at the Fermi level, the parallel dispersion and energies are similar to those of the clean substrate. This is also the case at higher coverages. Therefore, the energy and dispersion of the substrate peaks are independent of the amount of deposited Ag. The most likely explanation for this behaviour is that photoemission probes the Ag(1 1 1) islands and the bare regions between the islands. Therefore, the valence band spectra are a simple superposition of the valence band spectra of the substrate and of the overlayer. However, there are some important changes, which arise from the interaction of Ag with TiS₂. We discuss this in detail below.

4.2.1. The intensity enhancement at E_F. The photoemission intensity at the Fermi level is strongly enhanced throughout the whole Brillouin zone. This becomes particularly clear near the zone boundary at M(L) ($\theta = 28°$). This enhancement supports the view that silver transfers charge to the dispersionless Ti 3d states. Also near the zone centre, the emission from the featureless state at the Fermi level is significantly enhanced. If the states at the Fermi level were true conduction band states, we might expect that the Fermi level moves upwards as the conduction band states become partially filled by charge transfer from the silver. This Fermi level shift would manifest itself by a rigid shift of all occupied valence band states towards higher binding energy, because in the photoemission experiment the Fermi levels of the sample and the spectrometer are aligned. However, we do not observe such a shift. Instead, we only observe a strong enhancement of the photoemission from the states at E_F. At first sight, it seems that the dispersionless state behaves like an acceptor-like impurity band. This has also previously been suggested by Schärli *et al* for Ti$_{1+x}$S₂ and Ti$_{1-x}$V$_x$S₂ [37]. However, the possibility that this state is due to many-body effects cannot be ruled out. Inspired by the recently published STM images of TiS₂ [39], we suggest that energy-resolved real-space images obtained by STM will probably be very elucidating.

From the above considerations, it is concluded that silver donates charge to the host. However, we have to distinguish between different types of Ag atoms. According to the RHEED patterns, silver immediately forms three-dimensional (1 1 1) clusters at the surface. On the other hand, the broadening of the substrate spots in LEED might suggest that, apart from large islands, silver is also present in very small nuclei or as a lattice gas. Finally, Ag atoms may also be intercalated. It is likely that Ag atoms in the bulk islands do not interact with the substrate. However, other types of Ag atoms, like those which
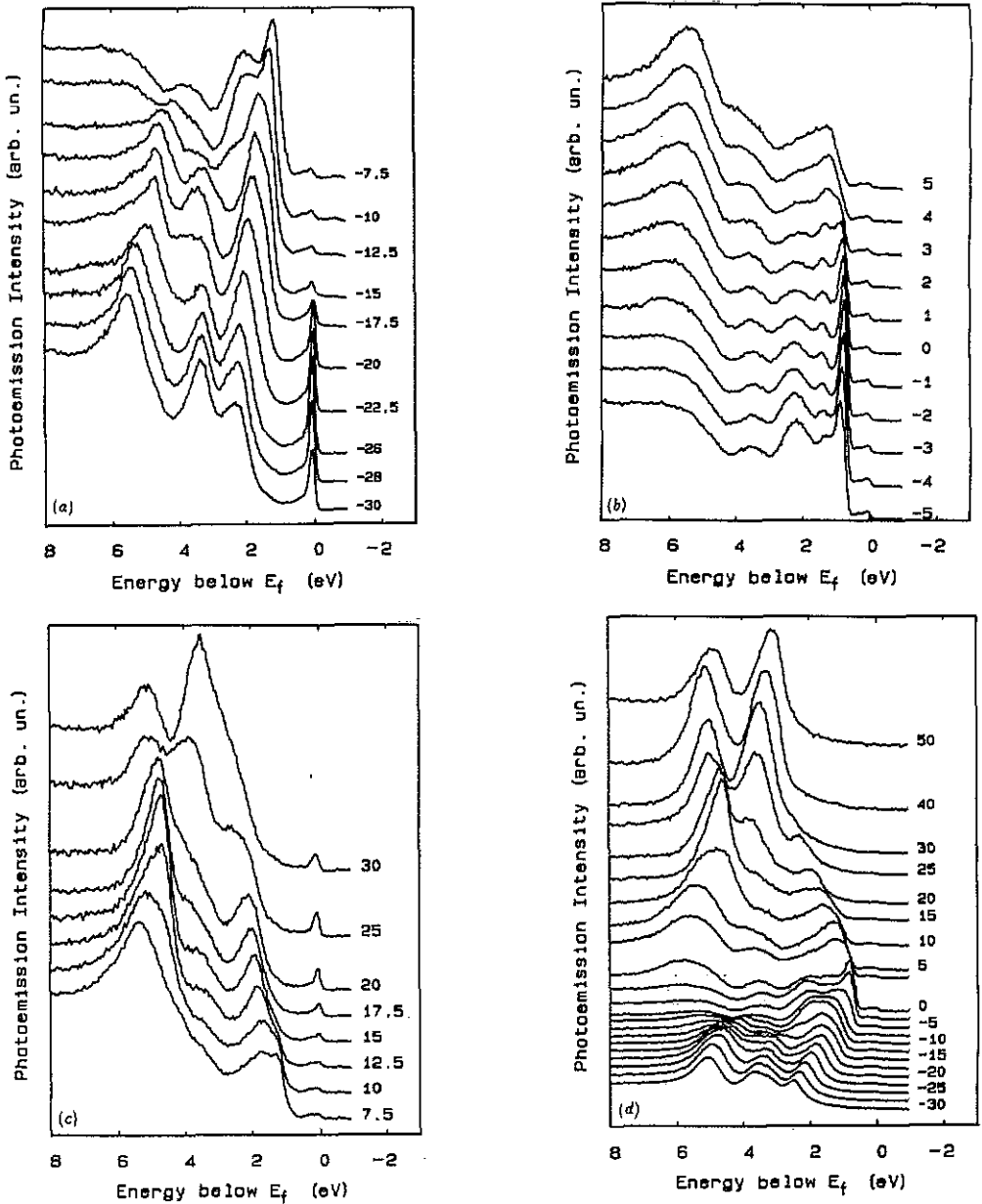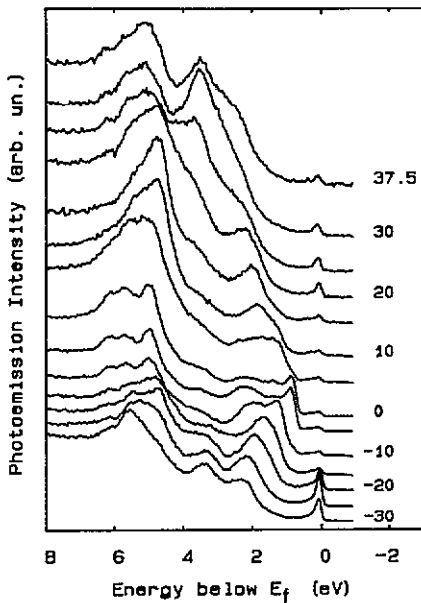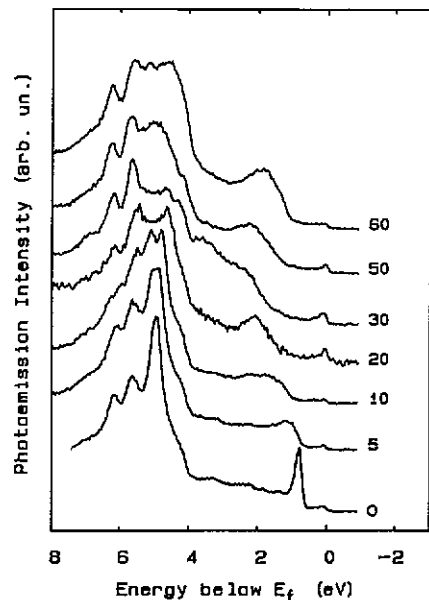
Figure 15. Angle-resolved He I spectra of Ag/TiS$_2$(001) along ΓMLA (a)-(c) and ΓKHA (d) after a deposition time of 1 min. The angle of light incidence is 45°. Emission angles are given in degrees. At this coverage, no Ag spots were visible in the LEED pattern.

constitute the interface between the substrate and the Ag islands or those which are present in small nuclei or are intercalated, will interact with TiS$_2$ and form covalent bonds. This probably also results in partial or complete transfer of the Ag 5s electrons to the 3d states of the substrate. We will argue below that probably most of the charge transfer originates from subsurface Ag.
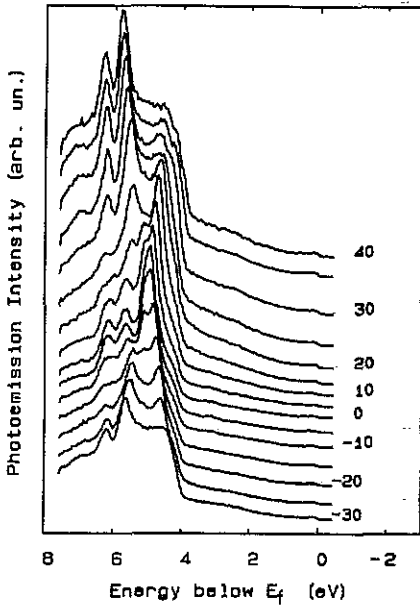
Figure 16. Angle-resolved He I spectra of Ag/ TiS$_2$(0 0 1) along ΓMLA after a deposition time of 2 min. The angle of light incidence is 45°. Emission angles are given in degrees. At this coverage, no Ag spots were visible in the LEED pattern.

**Figure 17.** Angle-resolved He I spectra of Ag/TiS$_2$(0 0 1) along ΓMLA after a deposition time of 30 min. The angle of light incidence is 15°. Emission angles are given in degrees. At this coverage, the LEED spots of Ag and of TiS$_2$ had approximately equal intensity.

On several occasions, the emission at E_F slowly increased in time after one particular evaporation event. Because intercalation is a time-dependent process, the enhanced d-band emission might be due to charge transfer from *intercalated* Ag atoms to the host. This intercalation was studied in more detail by AES (figure 19). It is seen that the intercalation process proceeds rather slowly. Because intercalation can only occur at lattice defects and steps, the intercalation rate will depend on the quality of the crystal surface. Starnberg and Hughes reached similar conclusions. They showed that, after different evaporation events, the Ag 4d emission intensity decreased rather fast due to intercalation. The Ti 3d emission intensity near the M point remained strong although almost all the silver diffused into the substrate. In other words, the Ti 3d emission intensity is nearly independent of the amount of Ag present at the surface. Therefore it is very likely that charge transfer to the Ti 3d band is from subsurface Ag. Additional evidence for charge donation from subsurface Ag will be provided by core-level photo-emission, which will be discussed in the next section.

On the other hand, charge transfer from intercalated Ag does not necessarily imply that surface Ag remains neutral. However, the occurrence of the Volmer–Weber growth mechanism indicates that the substrate–adsorbate interaction is weak, because, in the case of a strong binding between substrate and adsorbate atoms, a commensurate two-dimensional overlayer should be formed. Unfortunately, with photoemission it is not possible to obtain *microscopic* information about the chemical binding or electronic structure at a deeply buried interface.

Figure 18. Angle-resolved He I spectra of Ag/TiS$_2$(0 0 1) along the ΓMLA plane of the Brillouin zone of TiS$_2$, after a deposition time of 60 min. The angle of light incidence is 45°. Emission angles are given in degrees. At this coverage, only Ag spots were present in the LEED pattern. The spectra are similar to those of the Ag(1 1 1) surface [43]
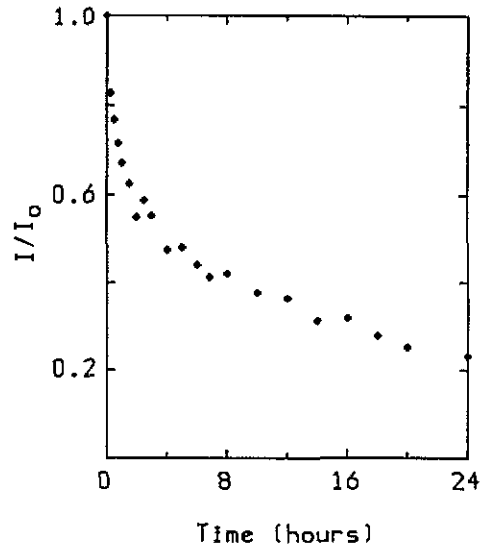
Figure 19. The Ag M$_{45}$VV Auger intensity as a function of time after deposition of three monolayers. The decrease of the Ag Auger intensity is due to intercalation. The ratio of the S and Ti Auger intensities remained constant.

4.2.2. Valence states near Γ. Together with the enhancement of the Ti 3d emission at M(L), a new peak appeared in the photoelectron spectrum. This peak is situated around Γ at about 1.4 eV below E_F. This peak was also observed by Starnberg and Hughes [14]. They also reported a downward shift of about 0.4 eV for the lowest photoemission peak near the M point. We do not observe such a shift. From the dispersion of all peaks at the Ag-covered surface (figure 11), it can be made plausible that this shift must be due to a small misalignment of the sample. This is quite conceivable, because the lowest valence band state is very dispersive near M. A comparison of the exact shape of their spectra and ours supports this view.

From figure 11 it is evident that, near Γ, the $Γ_2^- - A_2^-$ band is split: a new band appears at about 1.4 eV below E_F while the original band is shifted towards higher binding energy. From the variation of the photoemission intensity with the angle of light incidence (figure 20) it is seen that, unlike the uppermost valence band, which has a strong in-plane character, this intercalation-induced peak must have z character. However, it also has appreciable intensity at near-normal incidence. Because the $Γ_2^- - A_2^-$ state is split in the photoelectron spectrum, it is likely that the dispersion perpendicular to the sandwiches is seriously altered after deposition of Ag. This is not unreasonable, because if silver diffuses into the substrate, the inter-sandwich distance will increase. Because the $Γ_1^+$ and $Γ_2^-$ states are composed of S 3p$_z$ orbitals, forming bonding and antibonding combinations between successive sandwiches, respectively, the splitting between these
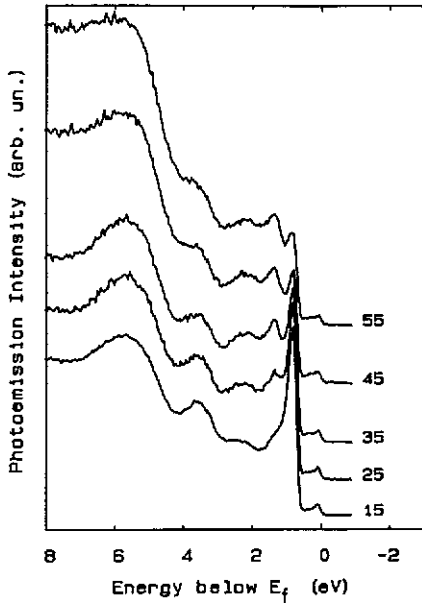
Figure 20. Normal He I emission spectra of Ag/TiS₂(0 0 1) at various angles of light incidence α. These spectra are obtained 24 h after a deposition event of 2 min.
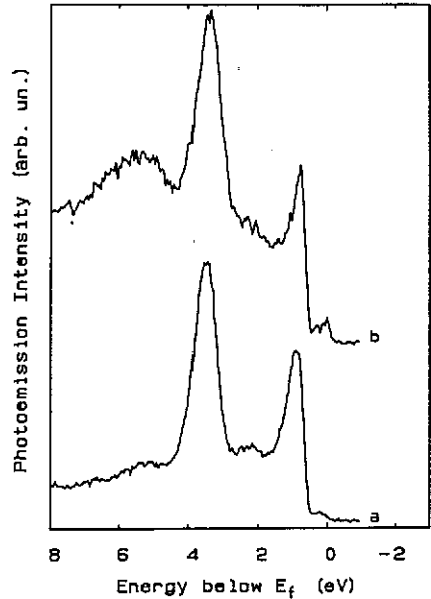
Figure 21. Normal He II emission spectra for clean TiS₂ (*a*) and Ag/TiS₂ (*b*). The angle of light incidence is 45°. These spectra are obtained 24 h after a deposition event of 2 min. The broad spectral feature at about 6 eV below E_f is due to emission from the Ag 4d states.

states should decrease as a result of intercalation. The A_1^+ and A_2^- states are antibonding and bonding, respectively, between the successive sandwiches. Therefore, the splitting between the A_1^+ and A_2^- states should increase, resulting in an overall decrease of dispersion along ΓA. Umrigar *et al* showed that the energy bands for a single TiS₂ sandwich are approximately the average of the bulk bands along the ΓMK and ALH directions [42]. Starnberg and Hughes [14] argued that the energy of the intercalation-induced peak is close to the centre of the ΓA band. This indicates that the inter-sandwich interaction must be very small after intercalation. However, the situation is more complicated because the presence of the intercalation-induced peak is not simply due to a shift of the $\Gamma_2^- - A_2^-$ derived peak, but rather points towards a splitting of the original peak. Because this must be due to three-dimensional effects, a detailed photon-energy-dependent photoemission study in Γ should be performed. We used Ne I and He II radiation but could not trace this intercalation-induced peak. This in turn indicates that it is important to study the perpendicular dispersion using a photon source having a continuous spectral distribution (synchrotron radiation).

We do not observe a similar splitting in the $\Gamma_1^+ - A_1^+$ derived peak. However, the situation may be complicated by overlap with emission from the Ag 4d states. The contribution from the Ag 4d states is clearly resolved in the He II spectrum (figure 21). Starnberg and Hughes reported that the photoemission intensity from the lowest valence band state in Γ is reduced upon Ag deposition. This might indicate that this state is involved in the bonding of silver to the substrate. To separate the contribution of the S
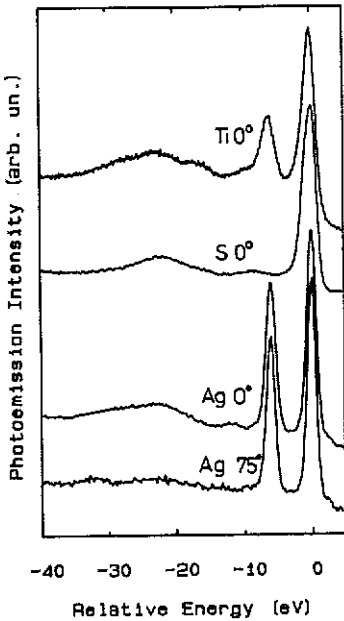
Figure 22. Angle-resolved XPS spectra ($\hbar\omega$ = 1253.6 eV) of the S and Ti 2p core levels in clean TiS$_2$ and the Ag 3d core levels after silver deposition and annealing (see text). Take-off angles of 0° and 75° with respect to the surface normal correspond to the bulk-sensitive and surface-sensitive modes, respectively. The broadening and shift of the Ag 3d core-level spectra at normal emission (see text) are too small to be observed on this scale.
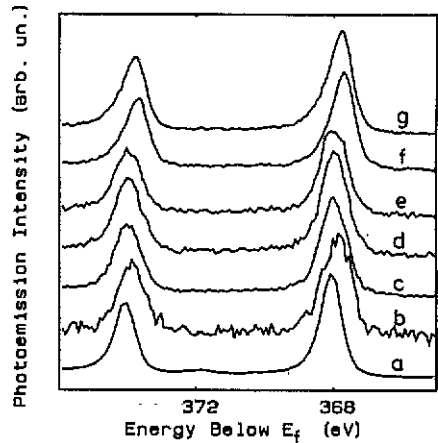
Figure 23. Detailed Ag 3d core-level spectra at normal emission after several deposition sequences (table 4).

3p and Ag 4d photoemission intensities, difference spectra should be obtained after each evaporation cycle. However, this method is prone to large errors when the sample has to be transported and realigned for each deposition sequence. Exploiting the photon-energy dependence of the photoionization cross sections, one might be able to disentangle the S and Ag contributions to the photoemission intensity by using synchrotron radiation.

Finally, we want to compare our results with the band-structure calculations on hypothetical AgTiS$_2$ [18]. According to these calculations, the Ag 4d states are strongly hybridized with the S 3p states, while the Ag 4d–Ti 3d interaction is very small. Upon intercalation, the top of the valence band is shifted from Γ to A, where it consists of an approximately equal amount of S 3p and Ag 4d characer. The p–d gap has disappeared. The Ag 5s band is well above the Fermi level and the Ti 3d band is partially filled. Our photoemission data also show that the Ti 3d states become partially filled. However, we do not have evidence that the p–d gap disappears. Possibly, the amount of intercalated Ag is too small, so that a comparison with hypothetical AgTiS$_2$ does not make sense. Also, experimentally, it is impossible to intercalate more than 0.42 Ag atoms per Ti atom, i.e. Ag$_{0.42}$TiS$_2$ [22].

5. Core-level spectroscopy

5.1. Angle-resolved x-ray photoelectron spectroscopy

Using the equipment for angle-resolved photoemission spectroscopy, we recorded the Ti 2p and S 2p core-level spectra of clean TiS$_2$ (figure 22). The energy resolution is about 1.1 eV. On the high-binding-energy side of the unresolved S 2p doublet, we observed two distinct energy-loss satellites at about 8 and 22 eV. Similar satellites were observed near the Ti 2p core-level spectra, but, owing to the spin–orbit splitting of the main peak, these satellite structures look more complicated. The origin of these satellites can be understood by a comparison with the optical reflection spectra and electron energy-loss spectra of TiS$_2$ [45].

The optical reflection spectrum of TiS$_2$ displays a rather broad band between 3 and 7 eV, which is due to S 3p–Ti 3d charge-transfer (interband) transitions. At about 8 eV, there is a large dip in the reflection spectrum. At this point, all charge-transfer transitions are exhausted and the onset of a plasma resonance is expected at this energy. This is consistent with a pronounced maximum in the energy-loss function $Im[-1/\varepsilon(q, \omega)]$ of TiS$_2$ at about 8 eV [45]. The region between about 10 and 16 eV is characterized by S 3s → Ti 3p and S 3p → Ti 4s, 4p, S 3d interband transitions. At a loss energy of about 22 eV, a high maximum in the energy-loss function is observed, which is attributed to a plasma resonance involving all 16 valence electrons. These distinct maxima in the energy-loss function are characteristic for a large number of layered transition-metal dichalcogenides [46]. We finally note that these satellites may be due to an intrinsic or extrinsic process. By extrinsic, we mean that the photoelectron may suffer several losses on its way through the solid, for example plasmon losses. By intrinsic, we mean that the core hole may be screened by ligand-to-metal charge transfer or by polarization of the ligands, giving rise to the so-called charge-transfer and exciton satellites, respectively. Also, plasmon excitations may be intrinsic. For a detailed discussion of these effects, we refer to de Boer *et al* [47].

Satellites in photoelectron spectra are useful for distinguishing surface and sub-surface Ag. After 5 min deposition of Ag onto TiS$_2$, followed by a mild heating of the sample (150 °C) for 2 h, we recorded Ag 3d core-level spectra in surface-sensitive and bulk-sensitive modes by varation of the detection angle (figure 22). At normal emission, similar energy-loss satellites as for the S or Ti core-level spectra are observed. These energy-loss satellites at the Ag 3d core spectra were also observed by Schärli and Brunner for Ag$_{0.12}$TiS$_2$ [48]. In our case, the Ag 3d core levels are shifted 0.2 eV towards *lower* binding energy as compared to those of a thick metallic overlayer. Also the full width at half-maximum (FWHM) increased 0.1 eV. In contrast, at an emission angle of 75° with respect to the surface normal, the satellite intensity is almost zero and the binding energy and the FWHM of the Ag 3d core spectra were identical to those at thick metallic overlayers. We conclude that, at grazing emission, mainly photoelectrons from surface Ag, present in epitaxial islands, are detected. At normal emission, also photoelectrons from intercalated Ag atoms are detected.

5.2. Core levels of Ag, Ti and S

We investigated the core-level spectra in more detail using a small-spot ESCA (electron spectroscopy for chemical analysis) apparatus with improved energy resolution (0.65 eV). The photon energy was 1486.6 eV. After different deposition events, we
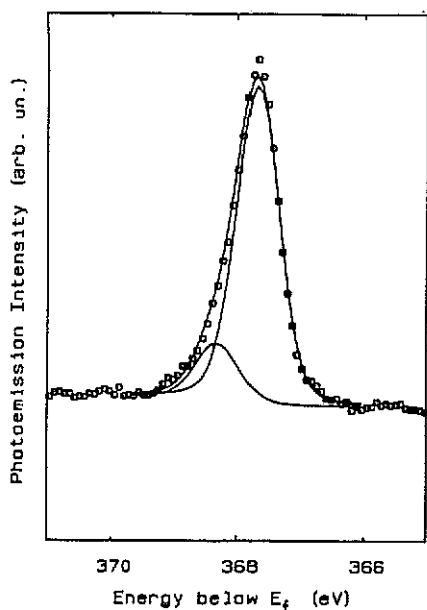
Figure 24. Fitting of the Ag $3d_{5/2}$ core-level spectrum of $Ag_{0.35}TiS_2$ with two Gaussians (FWHM = 0.7 eV), originating from surface and subsurface Ag. See also table 4.

determined the surface chemical composition with XPS. We also measured the substrate and adsorbate core levels after deposition of Na or K on clean TiS_2. Finally, by exploiting the small spot size of our x-ray source, we were able to record the core-level spectra of a cleaved $Ag_{0.35}TiS_2$ crystal. The results are listed in tables 4 and 6.

5.2.1. Ag 3d core levels. First we will have a closer look at the Ag 3d core-level spectra. In figure 23 spectrum (*a*) is recorded for a thick metallic overlayer and serves as a reference for binding energies and peak widths.

After successive evaporation events (spectra (*b*)–(*e*)), the Ag 3d core-level spectra have shifted and broadened as compared to spectrum (*a*). Spectrum (*f*) is obtained after prolonged annealing at about 200 °C. This spectrum is remarkably similar to spectrum (*g*), which is the Ag 3d core-level spectrum of a single-crystal $Ag_{0.35}TiS_2$. A comparison with spectrum (*a*) shows that the core-level spectra (*f*) and (*g*) are shifted 0.2 eV towards lower binding energy. In both spectra, we also observed strong plasmon satellites on the high-binding-energy side. This proves that the Ag 3d core levels in spectra (*f*) and (*g*) belong to subsurface Ag. The shoulder on the high-binding-energy side in spectra (*f*) and (*g*) is probably due to a small amount of Ag that is still present at the surface. In fact, each peak in the spectra (*b*)–(*g*) can be fitted by a superposition of two peaks, having a FWHM of 0.7 eV like the Ag peaks in spectrum (*a*) (figure 24). It is obvious that the component at higher binding energy corresponds to surface Ag, while the component at lower binding energy corresponds to subsurface Ag. From table 4, it is clear that the total Ag photoemission intensity remains approximately the same after several evaporation events ((*c*)–(*e*)). This proves that Ag diffuses into the substrate. Particular, after the first evaporation event (*b*), most of the Ag diffused into the substrate. After the second evaporation event, more Ag remains at the surface and forms epitaxial Ag(1 1 1) crystallites.

Table 4. Percentages of the Ag photoemission intensity after several evaporation events. The sum of the S, Ti and Ag intensities is 100%. The intensities are corrected for cross sections and analyser transmission. The photoemission intensities from surface and subsurface Ag are determined by fitting the Ag $3d_{5/2}$ core-level spectrum with two Gaussians having a FWHM of 0.7 eV. Binding energies E_B are also determined from these fits. Spectrum (a) corresponds to a thick, bulk-like metallic overlayer. See also figure 24.

Spectrum	Deposition time (s)	Ag (%)	Surface Ag (%)	E_B (eV)	Subsurface Ag (%)	E_B (eV)
(a)	3600	100	100	368.1		
(b)	10	6	2	368.4	4	367.8
(c)	20	18	7	368.3	11	367.9
(d)	30	18	10	368.2	8	367.8
(e)	50	20	8	368.3	12	367.8
(f)	*ᵃ	7	1	368.3	6	367.7
(g)	*ᵃ	29	5	368.4	24	367.8

ᵃ After prolonged annealing (12 h) at 200 °C.
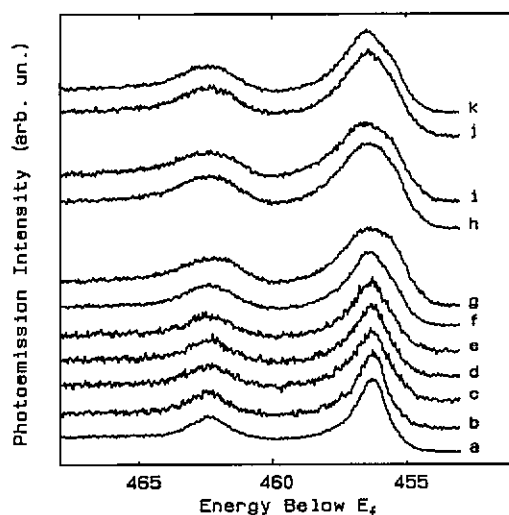
Figure 25. Ti 2p core-level spectra of clean TiS₂(a), Ag₀.₃₅TiS₂(g) and after deposition of Ag (b–f) or after deposition of Na (h, i) and K (j, k). For surface compositions, see tables 4 and 6.

At first sight, the 3d core-level shift from intercalated Ag to lower binding energy may seem remarkable, because intercalated Ag transferred charge to the Ti 3d states and must be present as positively charged ions. Therefore, one expects that the 3d core levels of intercalated Ag will shift towards higher binding energy. However, this chemical shift will be reduced by the polarization of the ligands, while the Madelung potential at the core-hole site may even change the direction of the energy shift. Therefore, it will be difficult to predict the final magnitude and direction of the energy shift.

5.2.2. Ti 2p core levels. We now turn to the Ti 2p core-level spectra (figure 25). These spectra show rather broad peaks with asymmetric lineshapes. The asymmetry arises from electron–hole excitations across the Fermi level and can be described by a Doniach–

Table 5. Fitting parameters for the Ti $2p_{1/2}$ core-level spectra. The Ti 2p core-level spectrum of clean TiS_2 probably corresponds to a poorly screened final state. I_p/I_w is the intensity ratio between the poorly screened peak (I_p) and the well screened peak (I_w). See also figure 26.

	Poorly screened final state		Well screened final state			
Spectrum	E_B (eV)	FWHM (eV)	E_B (eV)	FWHM (eV)	α	I_p/I_w
(a)	456.1	0.56			0.16	
(f)	456.6	1.18	455.8	1.0	0.19	1.4
(g)	456.7	1.48	455.6	0.84	0.27	2.5

Sunjic lineshape [49]. After incorporating a Lorentzian lifetime broadening, the photo-electron spectrum $F(E)$ is given by a convolution of $1/E^{1-\alpha}$ a Lorentzian having a FWHM of 2γ:

$$F(E) = \frac{\Gamma(1 - \alpha)\cos[\pi\alpha/2 + (1 - \alpha)\tan^{-1}(E/\gamma)]}{(E^2 + \gamma^2)^{(1-\alpha)/2}} \tag{7}$$

where Γ denotes the Γ-function and α the asymmetry parameter, which is proportional to the square of the local density of states at E_F on the core-hole site.

In order to fit the photoelectron spectrum with the Doniach–Sunjic lineshape, we first corrected the spectrum for the transmission of the analyser, which is inversely proportional to the kinetic energy of the electrons, and subtracted the background using [50]

$$I(E_n) = I_m(E_n) - \beta \int_{E_n}^{E_c} I(E)\, dE \tag{8}$$

where $I(E_n)$ and $I_m(E_n)$ are the corrected and the measured intensity, respectively, at kinetic energy E_n. The proportionality constant β is determined by iteration. E_c is the high-kinetic-energy cut-off of the spectrum.

After a convolution of equation (7) with a Gaussian distribution function (FWHM = 0.65 eV), which accounts for the instrumental broadening, the Ti 2p spectrum of TiS_2 was fitted using a non-linear least-squares fitting procedure. The binding energy, Lorentzian FWHM and the asymmetry parameters were taken as free parameters. A listing of parameters is given in table 5. Figure 26 shows the experimental spectra fitted by the theoretical lineshapes (full curves). The agreement is quite satisfactory. The non-zero asymmetry parameter indicates that Ti 3d states are present at the Fermi level.

After Ag deposition, the Ti 2p core-level spectra become very broad and, in some cases, a weak shoulder is recognizable on the low-binding-energy side. This suggests that the peak broadening is due to overlap of different components in the Ti 2p spectra. Indeed, these spectra cannot be fitted with a single broadened Doniach–Sunjic lineshape. This might be due to an initial-state effect. For example, if the d states become partially occupied, we may have an overlap of $Ti^{4+}(3d^0)$ and $Ti^{3+}(3d^1)$ components. However, this is not very likely because the 3d electrons in TiS_2 intercalates are itinerant and do not show a hopping behaviour. Another possible initial-state effect would be that the Ti sites become inequivalent after intercalation. Because we do not know how the intercalated metal is distributed between the sandwiches, we do not rule out this possibility. On the other hand, Fujimori *et al* argued that the broadening of the Ti 2p
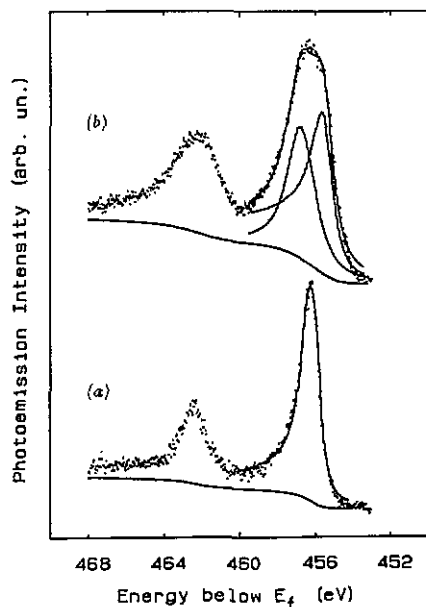
Figure 26. Least-squares fit of the Ti $2p_{3/2}$ core-level spectrum of (a) TiS_2 and (b) $Ag_{0.35}TiS_2$. For TiS_2, the spectrum is fitted with a Doniach–Sunjic lineshape (equation (7)), convoluted with a Gaussian with a FWHM of 0.65 eV. For $Ag_{0.35}TiS_2$, the spectrum is fitted by a superposition of a Lorentzian and a Doniach–Sunjic lineshape, convoluted with a Gaussian (FWHM = 0.65 eV), representing the poorly screened and well screened final states. For parameter values, see table 5.
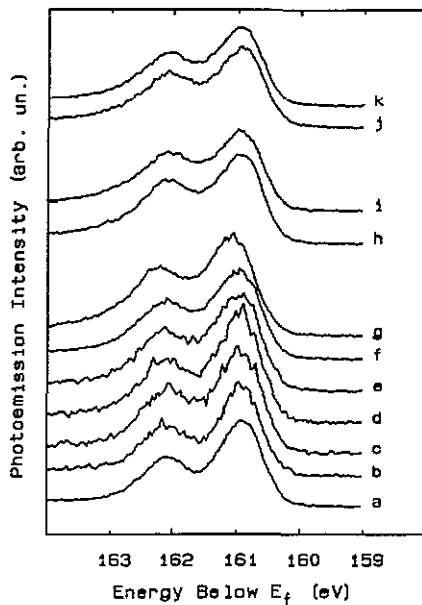
Figure 27. Sulphur 2p core-level spectra at different surface compositions (table 6).

core-level spectra in 3d transition-metal intercalates of TiS_2 is due to a final-state effect [51]. Two possible final states were considered, one in which an initially unoccupied Ti 3d level is pulled down below the Fermi level by the core-hole potential and becomes occupied. This situation corresponds to a well screened final state and gives rise to a photoemission peak with an asymmetric lineshape shifted towards lower binding energy [52]. Another possibility is that this screening level remains empty. In that case, the 3d hole has a finite lifetime and the poorly screened final state corresponds to a Lorentzian broadened peak shifted towards higher binding energy [52].

Spectra (f) and (g) were fitted with two different components, reflecting the well screened and the poorly screened final state. The fitting parameters are given in table 5. The overall agreement of the fit is very good, except for a small tail on the low-binding-energy side (figure 26). After convolution with a Gaussian having a FWHM of about 1 eV, this small discrepancy is removed. However, there exists no physical basis for increasing the FWHM of the Gaussian function beyond the instrumental resolution.

We are aware of the fact that one must be careful in interpreting the parameter values because a large number of parameters are involved. However, we observe similar trends as Fujimori *et al* for the 3d transition-metal intercalates of TiS_2. The asymmetry parameter α and the FWHM of the poorly screened peak increase with Ag concentration.

Table 6. Fitting parameters for the S 2p core-level spectra at different surface compositions. In contrast to table 4, spectrum (*a*) belongs to the clean surface. The spectra labelled (*b*)–(*g*) are recorded from the same samples as in table 4. In all cases, the ratio of the Ti and S concentrations was 0.50 ± 0.05. The experimental errors in the binding energies are about 0.05–0.1 eV.

Spectrum	Adsorbate	Surface composition (%)	S 2p$_{3/2}$		S 2p$_{1/2}$	
			E_B (eV)	FWHM (eV)	E_B (eV)	FWHM (eV)
(*a*)	–	–	160.89	0.8	162.06	0.9
(*b*)–(*e*)	Ag	*^{a}	160.92	0.8	162.05	0.9–1.1
(*f*)	Ag	*^{a}	160.93	0.8	162.06	1.2
(*g*)	Ag	*^{a}	161.04	0.8	162.18	1.1
(*h*)	K	10.2	160.90	0.8	162.03	1.1
(*i*)	K^b	12	160.89	0.8	162.00	1.2
(*j*)	Na	15	160.90	0.8	162.02	1.1
(*k*)	Na^b	17	160.91	0.7	162.02	1.2

^{a} See table 4.
^{b} After prolonged annealing (12 h) at 200 °C.

This is compatible with the view that the number of Ti 3d conduction electrons increases with Ag content. The increase of α is due to the increased density of states at the Fermi level. Fujimori *et al* argued that the increased lifetime broadening of the poorly screened final state is related to the increased decay rate of the Ti 3d hole in the screening level, as the number of conduction electrons increases. The energy separation between the well screened and poorly screened peaks is equal to the Coulomb interaction energy between the 2p core hole and the Ti 3d electron, and is about 1 eV in Ag$_{0.35}$TiS$_2$. According to Fujimori *et al* [51], well screened peaks are weak in the case of pure TiS$_2$, because the Ti 3d conduction band is almost empty.

We finally note that a similar broadening of the Ti 2p core-level spectra is observed immediately after deposition of Na and K. After successive evaporations, the K and Na concentration at the surface remained very small. Even after prolonged annealing, the surface concentrations of Na or K remained approximately the same (table 6). From our RHEED data, we already concluded that the alkali atoms intercalated very rapidly. Therefore, it is very likely that we measured intercalated Na or K with XPS. This is confirmed by the strong broadening of the Ti 2p core-level spectra immediately after deposition. The core-level binding energies of the K 2p$_{3/2}$ and Na 1s core levels are 292.9 and 1071.4 eV, respectively.

5.2.3. S 2p core levels. The S 2p core levels are shown in figure 27 (see also table 6). From spectrum (*a*) to (*g*), we observe a shift to higher binding energy, which amounts to about 0.15 eV in spectrum (*g*). Again, the core-level spectra show an increase in asymmetry and FWHM. The S 2p spectra were fitted by a superposition of two Gaussians. The parameters are given in table 6.

The intensity ratio of these two Gaussian lines severely deviates from the theoretical branching ratio of the 2p spin–orbit double (1:2). We therefore attempted to fit the S 2p core levels with a Doniach–Sunjic lineshape, but the agreement was not very satisfactory. The increase in FWHM of the S 2p$_{1/2}$ core-level spectrum with adatom concentration might be due to a deterioration of the substrate surface caused by intercalation. Indeed, after mild sputtering of the clean substrate, we observed a similar asymmetry.

The increase in binding energy with Ag content is possibly due to a chemical shift arising from the S 3p–Ag 4d interaction. It may also be due to the filling of the Ti 3d band, which results in an increased Fermi energy of $Ag_{0.35}TiS_2$ as compared to TiS_2. This effect is also expected to be present after Na and K deposition. However, after alkali-metal deposition, the S 2p core levels do not show such a pronounced shift to higher binding energy. The different binding energies after Ag or alkali-metal depositions may be due to the fact that the Fermi-level shift is small in all cases while the valence bands of TiS_2 are much less affected by alkali intercalation than by Ag intercalation.

6. Summary and conclusions

Ag grows in (1 1 1) oriented three-dimensional islands on $TiS_2(0 0 1)$ with $Ag[1\bar{1}0]$ $\|TiS_2[1 0 0]$. The lattice mismatch is 15% and the Ag overlayer is fully incommensurate. So it is likely that this lattice mismatch is not an important parameter for the occurrence of epitaxial growth. We have shown that RHEED is more suitable to study small islands than LEED. The absence of adsorbate reflections in the LEED pattern may lead to the wrong impression that Ag grows in registry with the substrate surface [14].

The structure and growth of Ag on TiS_2 are characteristic for systems howing little substrate–adsorbate interaction. Similar behaviour was reported for other metal–layered compound systems [8]. However, we would like to stress that none of the surface science techniques is very suitable for obtaining direct information about the structure and bonding at the interface between the three-dimensional clusters and the layered substrate. At the interface, relaxations may be present as the adatoms at the interface experience the substrate corrugation potential.

Angle-resolved UPS data and core-level spectroscopy data yield a consistent view that intercalation of monovalent metals is accompanied by a charge transfer to the 3d band of TiS_2. However, from our photoemission data it is not clear whether the charge transfer is complete, i.e. one electron per intercalated atom.

Na and K do not form three-dimensional metallic clusters on $TiS_2(0 0 1)$. Instead, Na and K atoms intercalate very rapidly. At $-140\,°C$, an ordered superstructure is observed for Na on $TiS_2(0 0 1)$. This might indicate that Na^+ ions are present at the surface. Coulomb interactions may lead to the formation of a $(\sqrt{3} \times \sqrt{3})R30°$ super-structure. However, charge transfer at the surface is not a necessary condition for the occurrence of ordering. The coverage of the $(\sqrt{3} \times \sqrt{3})R30°$ superstructure is probably one-third of a monolayer, although it was not possible to measure the coverage because the alkali atoms diffused very rapidly into the substrate.

Acknowledgments

References

[1] Mooser E (ed) 1976–79 *Physics and Chemistry of Materials and Layered Structures* vol 1–6 (Dordrecht: Reidel)

[2] Koma A and Yoshimura K 1986 *Surf. Sci.* **174** 556

[3] Pashly D W 1965 *Adv. Phys.* **14** 327

[4] Bermond J M and Venables J A 1983 *J. Cryst. Growth* **64** 239

[5] Hughes G J, McKinley A, Williams R H and McGovern I T 1982 *J.Phys. C: Solid State Phys.* **15** L159

[6] McGovern I T, Dietz E, Rotermund H H, Bradshaw A M, Braun W, Radlik W and McGilp J F 1985 *Surf. Sci.* **152/153** 1203

[7] Lince J R, Darré D J and Fleischauer P D 1987 *Phys. Rev.* B **36** 1647

[8] Jaegermann W, Pettenkofer C and Parkinson B A 1990 *Phys. Rev.* B **42** 7487

[9] Ohuchi F S, Jaegermann W, Pettenkofer C and Parkinson B A 1989 *Langmuir* **5** 439

[10] Jaegermann W, Ohuchi F S and Parkinson B A 1988 *Surf. Sci.* **201** 211

[11] Bortz M L, Ohuchi F S and Parkinson B A 1989 *Surf. Sci.* **223** 285

[12] Bauer E and Poppa H 1972 *Thin Solid Films* **12** 167

[13] Christman K and Ertl G 1975 *Thin Solid Films* **28** 3

[14] Starnberg H I and Hughes H P 1987 *J. Phys. C: Solid State Phys.* **20** 4429

[15] Hibma T 1982 *Intercalation Chemistry* ed M S Wittingham and A J Jacobson (New York: Academic)

[16] Friend R H and Yoffe A D 1987 *Adv. Phys.* **36** 1

[17] Ref [1], vol 3

[18] Dijkstra J, van Bruggen C F and Haas C 1989 *J. Phys.: Condens. Matter* **1** 4297

[19] Chen C H, Fabian W, Brown F C, Woo K C, Davies B and DeLong B 1980 *Phys. Rev.* B **21** 615

[20] Barry J J, Hughes H P, Klipstein P C and Friend R H 1983 *J. Phys. C: Solid State Phys.* **16** 393

[21] Starnberg H I and Hughes H P 1987 *J. Phys. C: Solid State Phys.* **20** L97

[22] This crystal was kindly put at our disposal by Professor G A Wiegers. For details about the preparation and physical properties of $Ag_{0.35}TiS_2$ single crystals, see: Gerards A G, Roede H, Haange R J, Boukamp B J and Wiegers G A 1984 *Synth. Met.* **10** 51

[23] Dench M P and Seah W A 1979 *Surf. Interface Anal.* **1** 2

[24] Zhu G, Zang A D, Williams E D and Park R L 1986 *Surf. Sci.* **172** 433

[25] Rao G H, Weitering H H and Hibma T 1991 *Surf. Sci* at press

[26] Prutton M 1983 *Surface Physics* 2nd edn (Oxford: Oxford University Press)

[27] Bouwmeester H J M 1988 *Thesis* University of Groningen

[28] Rouxel J 1976 *Physics and Chemistry of Materials with Layered Structures* vol 6 ed F Levy (Dordrecht: Reidel) p 201

[29] Plummer E W and Eberhardt W 1982 *Adv. Chem. Phys.* **49** 533

[30] Grandke T, Ley L and Cardona M 1978 *Phys. Rev.* B **18** 3847

[31] Coehoorn R 1985 *PhD Thesis* University of Groningen

[32] Zunger A and Freeman A J 1977 *Phys. Rev.* B **16** 906

[33] Coehoorn R, Haas C, Dijkstra J, Flipse C J F, de Groot R A and Wold A 1987 *Phys. Rev.* B **35** 6195

[34] Smith N V and Traum M M 1975 *Phys. Rev.* B **11** 2087

[35] de Boer D K G, van Bruggen C F, Bus G W, Coehoorn R, Haas C, Sawatzky G A, Myron H W, Norman D and Padmore H 1984 *Phys. Rev.* B **29** 6797

[36] Drube W, Schäfer I and Skibowski M 1987 *J. Phys. C: Solid State Phys.* **20** 4201

[37] Schärli M, Brunner J, Vaterhaus H P and Lévy F 1983 *J. Phys. C: Solid State Phys.* **16** 1527

[38] Ettema A R H F 1990 unpublished results

[39] van Bakel G P E M, de Hosson J Th M and Hibma T 1990 *Appl. Phys. Lett.* **56** 2402

[40] Pehlke E and Schattke W 1987 *Z. Phys.* B **66** 31

[41] Dijkstra J 1990 private communication

[42] Umrigar C, Ellis D E, Ding-sheng Wang, Krakauer H and Posternak M 1982 *Phys. Rev.* B **26** 4935

[43] Yeh J J and Lindau I 1985 *At. Data Nucl. Data Tables* **32** 1

[44] Liebowitz D and Shevchik N J 1978 *Phys. Rev.* B **17** 3825

[45] Feldkamp L A, Shinozaki S S, Kukkonen C A and Faille S P 1979 *Phys. Rev.* B **19** 2291

[46] Bell M G and Liang W Y 1976 *Adv. Phys.* **25** 53

[47] de Boer D K G, Haas C and Sawatzky G A 1984 *Phys. Rev.* B **29** 4401

[48] Schärli M and Brunner J 1983 *Solid State Commun.* **45** 305

[49] Doniach S and Sunjic M 1970 *J. Phys. C: Solid State Phys.* **3** 285

[50] Antonides E 1977 *PhD Thesis* University of Groningen

[51] Fujimori A, Suga S, Negishi H and Inoue M 1988 *Phys. Rev.* B **38** 3676

[52] Kotani A and Toyozawa Y 1974 *J. Phys. Soc. Japan* **37** 912